

# PhocoSpace: An open-source simulation package to implement photoacoustic spatial coherence theory

Michelle T. Graham\* and Muyinatu A. Lediju Bell\*<sup>†‡</sup>

\*Department of Electrical and Computer Engineering, Johns Hopkins University, Baltimore, MD

<sup>†</sup>Department of Biomedical Engineering, Johns Hopkins University, Baltimore, MD

<sup>‡</sup>Department of Computer Science, Johns Hopkins University, Baltimore, MD

**Abstract**—We previously developed a novel photoacoustic spatial coherence theory and demonstrated its ability to model and optimize a wide range of photoacoustic short-lag spatial coherence (SLSC) imaging parameters, target geometries, and light profile sizes. Recognizing the broad potential of this theoretical application, we developed PhocoSpace, an open-source toolbox to simulate the coherence of photoacoustic signals correlated in the transducer space dimension. PhocoSpace is provided as a MATLAB extension, and this paper serves as an introductory user manual containing tutorials to illustrate toolbox capabilities. Target geometries, fluence distributions within an imaging plane, and parameters describing acoustic receivers (e.g., transducer element pitch, bandwidth, aperture size) may each be customized to model experimental setups, clinical scenarios, and imaging equipment specifications. We demonstrate that PhocoSpace is a flexible *in silico* tool to predict photoacoustic spatial coherence functions, determine expected photoacoustic SLSC image quality, and characterize multiple possible coherence-based photoacoustic image optimizations without requiring lengthy experimental data acquisition. In addition, this software package establishes a foundation for future investigations into alternative photoacoustic spatial coherence-based signal processing methods.

## I. INTRODUCTION

Photoacoustic imaging relies on the photoacoustic effect, which is initiated by pulsed light incident on an optically absorbing target generating an acoustic wave through thermal expansion followed by contraction. By tuning the wavelength of the incident light to maximize the optical absorption of a target of interest, chromophores (e.g., hemoglobin in blood, lipids in atherosclerotic plaques) can be selectively visualized with high contrast [1]. However, amplitude-based photoacoustic images tend to suffer from poor image quality when there is insufficient fluence at the target depth.

Spatial coherence-based imaging techniques have been introduced to improve amplitude-based photoacoustic image quality. The majority of these techniques weight the amplitude image by measured spatial coherence values [2]–[8]. Short-lag Spatial Coherence (SLSC) beamforming, a technique initially developed for ultrasound imaging [9], differs by directly displaying measured spatial coherence values to generate an image that is independent of signal amplitude. As a result, SLSC beamforming of photoacoustic images in high noise environments demonstrates notable improvements in contrast and signal-to-noise ratios, in comparison to traditional delay-and-sum beamforming [10]–[16].

To systematically characterize these and other empirical observations surrounding the photoacoustic SLSC beamformer,

we developed a photoacoustic-specific spatial coherence theory [17]. We then implemented our theory with simulations, followed by validation with experimental data from multiple photoacoustic target sizes and incident fluence profiles. In addition, we demonstrated that these simulations were useful to study a wide range of potential optimizations that would otherwise require lengthy experimental testing.

To maximize the full potential of our recently introduced spatial coherence theory, we developed PhocoSpace, an open-source toolbox to simulate and characterize multiple possible coherence-based photoacoustic image optimizations, with additional possible uses described in [18]. PhocoSpace is implemented as a MATLAB-based simulation package available at <https://gitlab.com/pulselab/phocospace>. This paper is organized as a user manual for PhocoSpace, beginning with a brief theoretical overview, followed by descriptions of the toolbox workflow with use case examples.

## II. PHOTOACOUSTIC SPATIAL COHERENCE THEORY

To develop the photoacoustic spatial coherence theory described in [17], the photoacoustic pressure field received by a transducer,  $P$ , is modeled as a linear system, defined as:

$$P(\mathbf{X}_0, \mathbf{X}_n, f) = \chi(\mathbf{X}_0, f)A_N(\mathbf{X}_0, f)H_{rx}(\mathbf{X}_0, \mathbf{X}_n, f), \quad (1)$$

where  $\chi$  is the random distribution of incoherent photoabsorbers,  $H_{rx}$  is the spherical propagation of the pressure wave from the source to a point on the transducer,  $f$  is the acoustic frequency, and  $\mathbf{X}_n$  is a point on the receiving aperture.  $A_N$  is the initial pressure distribution of absorbers located at position  $\mathbf{X}_0$  in the presence of noise and is defined as:

$$A_N = \begin{cases} \mu_a \Gamma F, & N_A = 0 \\ \mu_a \Gamma F + \langle \mu_a \Gamma F \rangle N_A, & N_A \neq 0 \end{cases} \quad (2)$$

where  $\langle \cdot \rangle$  represents the expected value and  $N_A$  is a zero-mean, Gaussian-distributed, additive noise term which originates from random fluctuation in the source distribution (e.g., variations in the fluence at the absorber surface [19] and variations in the optical absorption within the absorber).

Photoacoustic spatial covariance,  $R_p$ , is defined as the correlation of the received pressure field at two lateral receiving positions  $\mathbf{X}_1$  and  $\mathbf{X}_2$ :

$$R_p(\mathbf{X}_1, \mathbf{X}_2, f) = \langle P(\mathbf{X}_1, f), P^*(\mathbf{X}_2, f) \rangle, \quad (3)$$

where  $P^*$  represents the complex conjugate of  $P$ .

Eqs. (1)-(3) are foundational to the derivation of the following description, which predicts that photoacoustic spatial coherence is expressed as a phase term multiplied by the Fourier transform of the initial pressure distribution squared and scaled by noise terms:

$$R_p(\mathbf{m}, \mathbf{x}_k, z, f) = \frac{e^{-(j2\pi\mathbf{x}_k\mathbf{m}f)/cz}}{z^2} \int_{-\infty}^{\infty} [\chi_o |\Gamma\mu_a F|^2 + 2\chi_o \cdot N_A (\Gamma\mu_a F)^2 + \chi_o N_o |\langle \Gamma\mu_a F \rangle|^2] e^{-(j2\pi\mathbf{x}\mathbf{m}f)/cz} d\mathbf{x} \quad (4)$$

where  $\chi_o$  is the average power of the absorber distribution,  $N_o$  is the variance of the Gaussian distribution of  $N_A$ ,  $x_k$  is the lateral shift between the lateral location of interest in the imaging plane and the center of the imaging plane,  $z$  is the depth in the imaging plane,  $c$  is the speed of sound, and  $m$  is the spatial lag between two elements on the receiving aperture.

To obtain a theoretical SLSC image, the dependence on the entire bandwidth of the transducer was included by performing the following three steps. First, Eq. (4) was integrated over wavelengths that correspond to the highest and lowest acoustic frequencies within the -6 dB bandwidth of a traditional

ultrasound transducer frequency response (i.e.,  $f_H$  and  $f_L$ , respectively, approximating equal weights for each wavelength). Second, the result was normalized by the value obtained at lag zero (i.e.,  $K(x_k, z)$ ). Finally, we integrated over the first  $M$  lags to obtain each pixel in the theoretical SLSC image. These three steps are defined by the equation:

$$\begin{aligned} SLSC_{pixel}(x_k, z) &= \frac{1}{K(x_k, z)} \int_0^M \int_{f_L}^{f_H} R_p(m', x_k, z, f') df' dm', \\ &\approx \frac{1}{K(x_k, z)} \sum_{m=1}^M \sum_{f=f_L}^{f_H} R_p(m, x_k, z, f). \end{aligned} \quad (5)$$

### III. PHOCO SPACE WORKFLOW

The PhocoSpace workflow is implemented in two stages: (1) definition of imaging plane properties, followed by (2) evaluation of photoacoustic spatial coherence theory. Fig. 1 illustrates these two stages for an 8 mm diameter circular blood vessel target, represented as a graphical representation alongside associated MATLAB code.

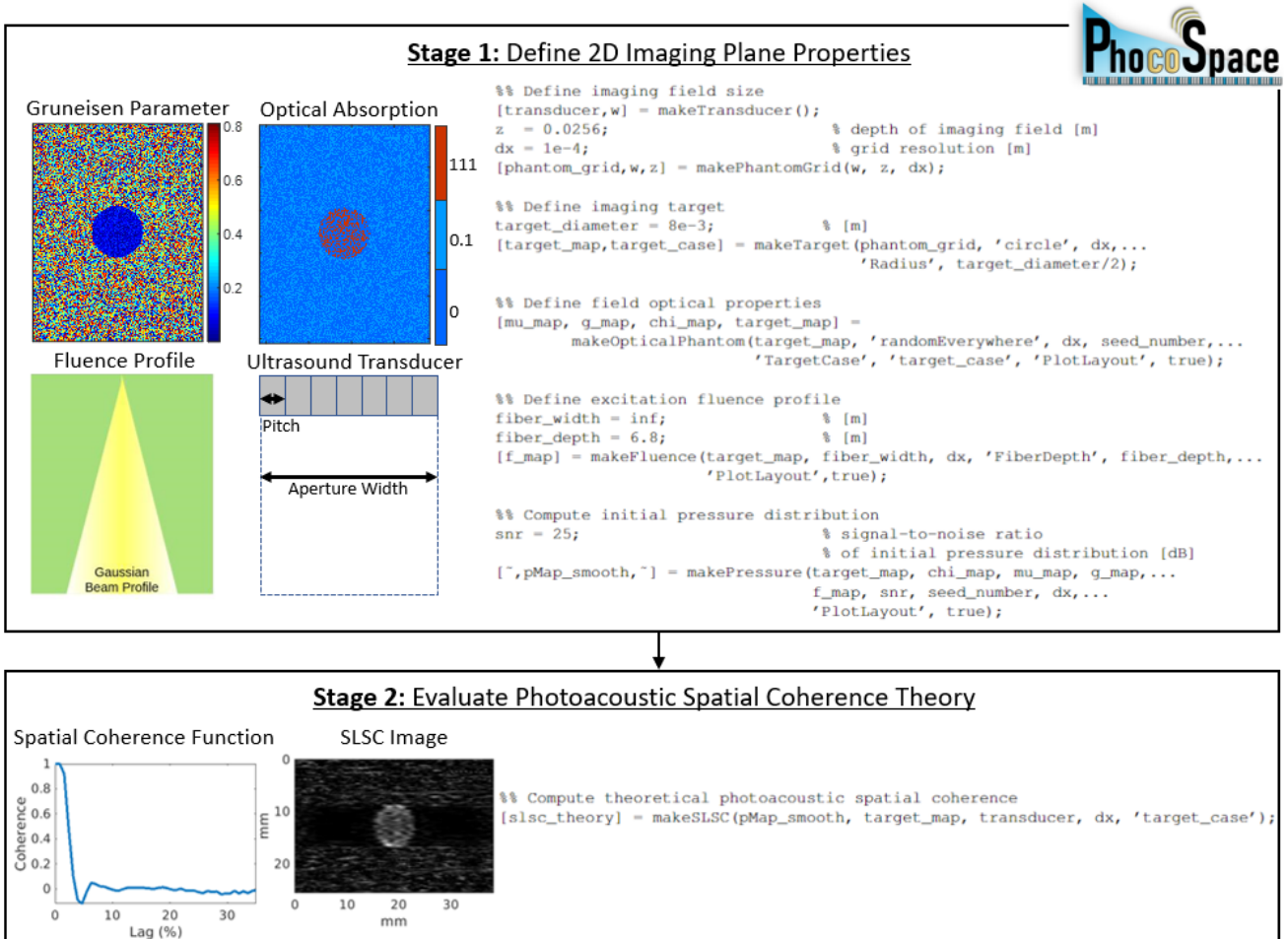


Fig. 1: Graphical illustration and associated MATLAB code demonstrating the two-stage PhocoSpace workflow for an 8 mm diameter circular blood vessel target.

TABLE I: Summary of the fields contained within the output structure, `slsc_theory`, which is generated by the theoretical photoacoustic spatial coherence and SLSC image computation executed with `makeSLSC.m`.

Field	Description
<code>N_ele</code>	Number of elements in transducer
<code>pitch</code>	Center-to-center distance between two transducer elements
<code>freq</code>	Transducer -6 dB bandwidth array
<code>x_axis</code>	Lateral image axis array
<code>z_axis</code>	Axial image axis array
<code>cc</code>	Computed coherence functions for each lateral location at an indicated depth and for each frequency in the field "freq"
<code>cc_avg</code>	Computed coherence functions for each lateral location at an indicated depth and averaged over the transducer bandwidth
<code>slsc</code>	Computed SLSC images for each M value and for each frequency in the field "freq"
<code>slsc_avg</code>	Computed SLSC images for each M value and averaged over the transducer bandwidth

In the first stage, the lateral dimension of the imaging plane corresponds to the lateral dimension of an ultrasound transducer, and the axial dimension corresponds to image depth. User-defined properties for Stage 1 include medium characteristics (e.g., target geometry, Grüneisen parameter, optical absorption) and properties of the imaging equipment (e.g., excitation fluence profile, transducer aperture width, transducer bandwidth, transducer pitch, variance of the additive Gaussian noise). The functions used to define these properties include `makeTransducer.m`, `makePhantomGrid.m`, `makeTarget.m`, `makeOpticalPhantom.m`, `makeFluence.m`, and `makePressure.m`.

In the second stage, the properties defined in the first stage are employed to evaluate Eqs. (4) and (5) to obtain theoretical spatial coherence functions and theoretical SLSC images, respectively. These computations are executed by the function `makeSLSC.m`. Table I summarizes the fields contained within the output structure `slsc_theory`.

#### IV. PHOCOSPACE USE CASES AND EXAMPLES

##### A. Default imaging properties and parameters

Customizations of PhocoSpace are demonstrated in the following sections, including modeling a diverse range of target geometries (Section IV-B), fluence profiles (Sections IV-C), and transducer bandwidths (Section IV-D). Unless otherwise noted, in each of these examples, the following eight default imaging plane definitions were employed as follows. First, an ultrasound transducer with 128 elements, 0.3-mm pitch, 3.84-cm total length, and -6 dB bandwidth of 3.75-7.0 MHz was placed at depth  $z = 0$  cm. Second, the fluence profile ( $F$ ) was a light sheet with a uniform fluence value of  $F = 5$  mJ/cm<sup>2</sup>, illuminating the entire phantom. Third, the optically absorbing targets were modeled as a distribution of randomly

positioned absorbers with a spatial density of 40 absorbers per mm<sup>2</sup> within the target region. Fourth, the mean magnitude of the optical absorption coefficient ( $\mu_a$ ) was 111 cm<sup>-1</sup> inside the photoacoustic target (to model hemoglobin in blood), 0.1 cm<sup>-1</sup> outside the target (to model tissue), and 0 cm<sup>-1</sup> when no absorbers were present [20], as illustrated in Fig. 1. Fifth, the Grüneisen parameter ( $\Gamma$ ) was modeled as random values ranging 0-0.81 and 0-0.144 in tissue and in blood, respectively [20], as illustrated in Fig. 1. Sixth, the average power of the absorber distribution,  $\chi_o$  was modeled as an arbitrary constant. Seventh, the variance ( $N_o$ ) of the added noise ( $N_A$ ) was  $8e^{-5}$ . Finally, the discrete set of frequencies indicating the -6 dB bandwidth of the frequency response of the transducer (i.e.,  $f_L = 3.25$  to  $f_H = 7.0$  MHz) were incremented using a fixed  $\Delta f = 0.25$  MHz. All SLSC images are displayed with  $M = 8\%$  of the receive aperture.

##### B. SLSC images of diverse target geometries

Fig. 2 shows the predicted SLSC images of the four example target geometries currently contained within the PhocoSpace package. These geometries include a 4 mm diameter circular target (`circle_4mm.mat`, Fig. 2(a)), a combination of six circular targets with diameters ranging 2-7 mm (`polkadots.mat`, Fig. 2(c)), a model of blood vessel vasculature [21] (`vasculature_kwave.mat`, Fig. 2(e)), and the Johns Hopkins University crest (`jhu_crest.mat`, Fig. 2(g)). Corresponding theoretical photoacoustic SLSC images produced by PhocoSpace are also shown. Overall, Fig. 2 demonstrates the flexibility of PhocoSpace to model a wide range of target geometries, and this example may be replicated using `demonstrate_target_maps.m` in the PhocoSpace package.

##### C. Multiple customizable fluence profiles

Fig. 3 demonstrates the predicted SLSC images of the six-circle target geometry (Fig. 2(c)) when excited with four fluence profiles. These profiles include the default light sheet with uniform fluence (Fig. 3(a)), as well as Gaussian profiles with 25 mm (Fig. 3(c)), 5 mm (Fig. 3(e)), and 1 mm (Fig. 3(g)) initial beam diameters, each with 6.8 mm initial depth. The Gaussian beam profiles were simulated using the light propagation model described in [17], [22]. The associated theoretical SLSC images demonstrate the portions of the target geometries visualized with each fluence profile. Fig. 3 can be replicated using the example `demonstrate_fluence_maps.m` in the PhocoSpace package.

Fig. 4 shows predicted theoretical coherence functions of the six-circle target geometry (Fig. 2(c)) when excited with four fluence profiles. Specifically, the coherence functions displayed are computed at the centers of the 2 mm and 7 mm diameter targets (Figs. 4(a) and 4(b), respectively). As stated in [17], two inverse relationships exist between (1) the lateral width of the target illuminated and the coherence length (i.e., the spatial lag coinciding with the first zero crossing of the coherence function), and (2) the target size and the coherence length. These relationships are mathematically dictated by

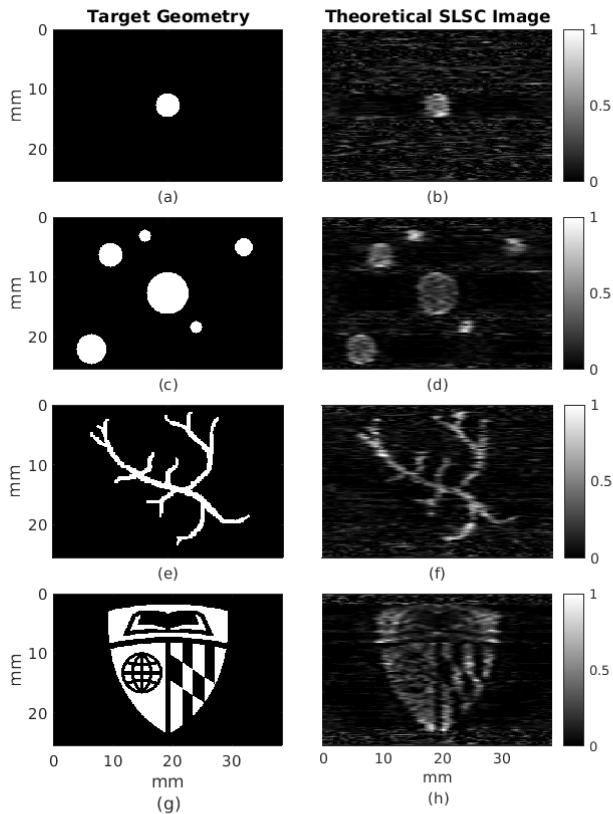


Fig. 2: Example photoacoustic imaging target geometries and associated theoretical SLSC images computed with PhocoSpace, including (a,b) a single 4 mm diameter target, (c,d) six circular targets with diameters ranging 2-7 mm, (e,f) a blood vessel vasculature model, and (g,h) the Johns Hopkins University crest.

the Fourier transform in Eq. (4), which can be considered as the van Cittert-Zernike theorem applied to photoacoustic imaging [17], [23], [24]. As the spatial frequency term of the Fourier transform in Eq. (4) is encoded in the x-axes of Fig. 4, these coherence functions confirm that increasing the width of the light profile or the target size (i.e., in the space dimension), decreases the coherence length (i.e., in the spatial frequency dimension). However, when the entire target width is illuminated, additional broadening of the light profile beyond the target width does not impact coherence length, as demonstrated by the overlapping coherence functions obtained with the light sheet and 25 mm Gaussian beam for each target.

Figs. 3 and 4 demonstrate that PhocoSpace successfully models multiple light profiles to investigate the effects of light illumination on photoacoustic spatial coherence functions and corresponding SLSC images.

#### D. Transducer bandwidth variations

Fig. 5 shows the predicted SLSC images of the vasculature geometry in Fig. 2(e), computed with -6dB transducer bandwidths of 8-17 MHz (Fig. 5(a)), 3-8 MHz (Fig. 5(b)), and 1-5 MHz (Fig. 5(c)). Fig. 5(d) shows corresponding lateral SLSC profiles (and the lateral target geometry profile) at the location indicated by the arrows in Fig. 5(a),

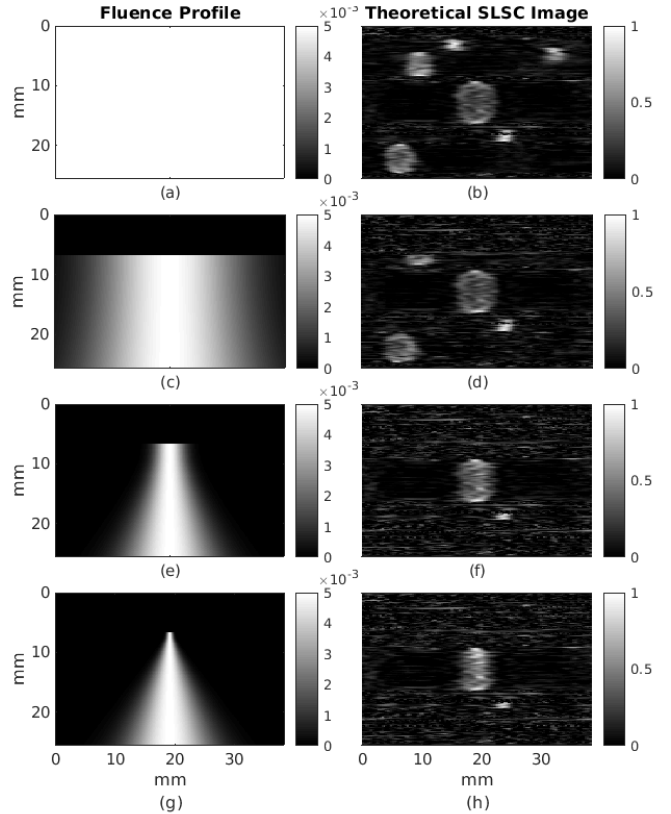


Fig. 3: Fluence profiles and corresponding SLSC images computed with PhocoSpace, including (a,b) a light sheet with a uniform fluence value of  $F = 5 \text{ mJ/cm}^2$  and Gaussian profiles with (c,d) 25 mm, (e,f) 5 mm, and (g,h) 1 mm initial beam diameters.

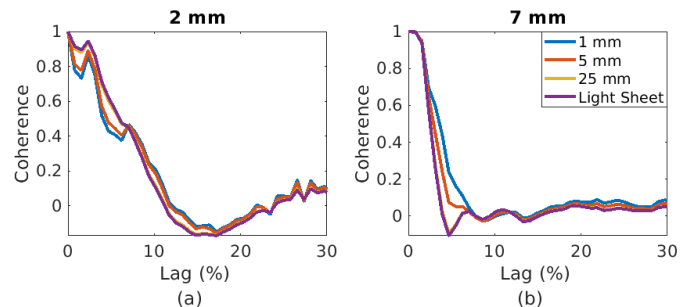


Fig. 4: Coherence functions extracted from the center of the (a) 2 mm diameter and (b) 7 mm diameter target in the six-circle target geometry when excited with the four fluence profiles shown in Fig. 3.

which corresponds to depth  $z = 8.1 \text{ mm}$ . Fig. 5 demonstrates that PhocoSpace successfully models the degradation of SLSC image resolution as transducer center frequency decreases, which is promising for additional customization based on common ultrasound transducer specifications. The output in Fig. 5 can be replicated using the example `demonstrate_transducer_bandwidth.m` in the PhocoSpace package.

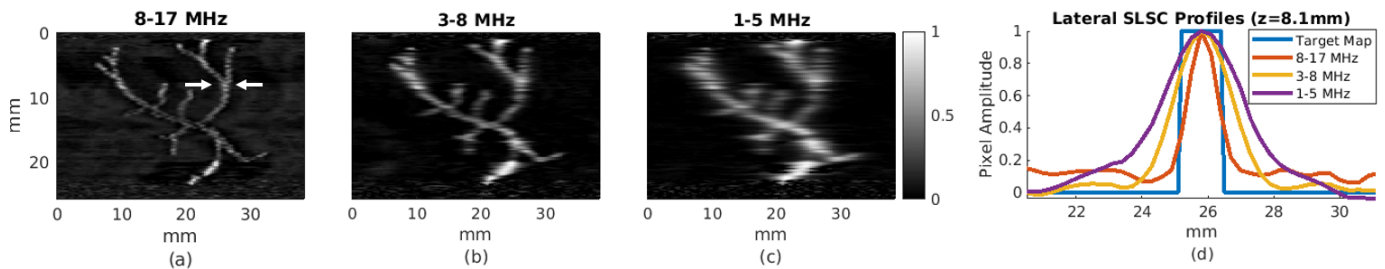


Fig. 5: SLSC images of the vasculature target geometry shown in Fig. 2, computed with transducer bandwidths of (a) 8-17 MHz (12.0 MHz center frequency), (b) 3-8 MHz (5.5 MHz center frequency), and (c) 1-5 MHz (3.0 MHz center frequency). (d) Corresponding lateral SLSC profiles at the location indicated by the white arrows, compared to a lateral profile taken from the same position within the vasculature target map geometry.

## V. CONCLUSION

Our previously derived photoacoustic spatial coherence theory established a foundation for exploration of coherence-based photoacoustic signal processing techniques without lengthy experimental testing. Based on this theory, we developed the PhocoSpace a simulation package to provide the imaging community with a flexible toolbox to execute and accelerate photoacoustic spatial coherence investigations. With customizable parameters (e.g., target geometry, incident light beam profile, transducer bandwidth), PhocoSpace is a promising approach to characterizing photoacoustic spatial coherence functions, photoacoustic SLSC images, and other coherence-based photoacoustic biomedical applications. Future innovations that require coherence-based photoacoustic techniques, analyses, and comparisons are additionally anticipated to benefit from this software release.

## ACKNOWLEDGMENTS

This research is supported by NSF CAREER Award ECCS 1751522 and NSF SCH Award IIS 2014088.

## REFERENCES

- [1] M. Xu and L. V. Wang, "Photoacoustic imaging in biomedicine," *Review of Scientific Instruments*, vol. 77, no. 4, p. 041101, 2006.
- [2] C. K. Liao, M. L. Li, and P. C. Li, "Optoacoustic imaging with synthetic aperture focusing and coherence weighting," *Optics Letters*, vol. 29, no. 21, pp. 2506–2508, 2004.
- [3] M.-L. Li, H. F. Zhang, K. Maslov, G. Stoica, and L. V. Wang, "Improved in vivo photoacoustic microscopy based on a virtual-detector concept," *Optics Letters*, vol. 31, no. 4, pp. 474–476, 2006.
- [4] S. Park, A. B. Karpouk, S. R. Aglyamov, and S. Y. Emelianov, "Adaptive beamforming for photoacoustic imaging," *Optics Letters*, vol. 33, no. 12, pp. 1291–1293, 2008.
- [5] Y. H. Wang and P. C. Li, "SNR-dependent coherence-based adaptive imaging for high-frame-rate ultrasonic and photoacoustic imaging," *IEEE Transactions on Ultrasonics, Ferroelectrics, and Frequency Control*, vol. 61, no. 8, pp. 1419–1432, 2014.
- [6] D. Wang, Y. Wang, Y. Zhou, J. Lovell, and J. X, "Coherent-weighted three-dimensional image reconstruction in linear-array-based photoacoustic tomography," *Biomedical Optics Express*, vol. 7, pp. 1957–1965, 2016.
- [7] S. Jeon, E.-Y. Park, W. Choi, R. Managuli, K. J. Lee, and C. Kim, "Real-time delay-multiply-and-sum beamforming with coherence factor for in vivo clinical photoacoustic imaging of humans," *Photoacoustics*, vol. 15, p. 100136, 2019.
- [8] E. J. Alles, M. Jaeger, and J. C. Bamber, "Photoacoustic clutter reduction using short-lag spatial coherence weighted imaging," in *2014 IEEE International Ultrasonics Symposium*. IEEE, 2014, pp. 41–44.
- [9] M. A. L. Bell, Trahey, G. E., Byran, B. C., and J. J. Dahl, "Short-lag spatial coherence of backscattered echoes: imaging characteristics," *IEEE Transactions on Ultrasonics, Ferroelectrics, and Frequency Control*, vol. 58, no. 7, pp. 1377–1388, 2011.
- [10] M. A. L. Bell, N. Ku, D. Y. Song, and E. M. Boctor, "Short-lag spatial coherence beamforming of photoacoustic images for enhanced visualization of prostate brachytherapy seeds," *Biomedical Optics Express*, vol. 4, no. 10, p. 1964, 2013.
- [11] M. A. L. Bell, N. P. Kuo, D. Y. Song, J. U. Kang, and E. M. Boctor, "In vivo visualization of prostate brachytherapy seeds with photoacoustic imaging," *Journal of Biomedical Optics*, vol. 19, no. 12, p. 126011, 2014.
- [12] M. A. L. Bell, D. Y. Song, and E. M. Boctor, "Coherence-based photoacoustic imaging of brachytherapy seeds implanted in a canine prostate," in *Medical Imaging 2014: Ultrasonic Imaging and Tomography*, vol. 9040. SPIE, 2014, pp. 166–171.
- [13] M. A. L. Bell, X. Guo, H. J. Kang, and E. Boctor, "Improved contrast in laser-diode-based photoacoustic images with short-lag spatial coherence beamforming," in *2014 IEEE International Ultrasonics Symposium*. IEEE, 2014, pp. 37–40.
- [14] B. Pourebrahimi, S. Yoon, D. Dopsa, and M. C. Kolios, "Improving the quality of photoacoustic images using the short-lag spatial coherence imaging technique," *Proceedings of SPIE Photonics West - Photons Plus Ultrasound: Imaging and Sensing 2013*, vol. 8581, 2013.
- [15] M. T. Graham, J. Huang, F. Creighton, and M. A. L. Bell, "Simulations and human cadaver head studies to identify optimal acoustic receiver locations for minimally invasive photoacoustic-guided neurosurgery," *Photoacoustics*, p. 100183, 2020.
- [16] E. A. Gonzalez and M. A. L. Bell, "GPU implementation of photoacoustic short-lag spatial coherence imaging for improved image-guided interventions," *Journal of Biomedical Optics*, vol. 25, no. 7, p. 077002, 2020.
- [17] M. T. Graham and M. A. L. Bell, "Photoacoustic spatial coherence theory and applications to coherence-based image contrast and resolution," *IEEE Transactions on Ultrasonics, Ferroelectrics, and Frequency Control*, vol. 67, no. 10, pp. 2069–2084, 2020.
- [18] M. A. L. Bell, "Photoacoustic vision for surgical guidance," in *2020 IEEE International Ultrasonics Symposium (IUS)*. IEEE, 2020, pp. 1–6.
- [19] B. Stephanian, M. T. Graham, H. Hou, and M. A. L. Bell, "Additive noise models for photoacoustic spatial coherence theory," *Biomedical Optics Express*, vol. 9, no. 11, 2018.
- [20] D. K. Yao, C. Yang, K. Maslov, and L. V. Wang, "Photoacoustic measurement of the grüneisen parameter of tissue," *Journal of Biomedical Optics*, vol. 19, no. 1, 2014.
- [21] B. E. Treeby and B. T. Cox, "k-Wave: MATLAB toolbox for the simulation and reconstruction of photoacoustic wave fields," *Journal of Biomedical Optics*, vol. 15, no. 2, p. 021314, 2010.
- [22] R. Fischer, B. Tadic-Galeb, and P. Yoder, *Optical System Design, Second Edition*. The McGraw-Hill companies, Inc., 2000.
- [23] R. Mallart and M. Fink, "The van Cittert-Zernike theorem in pulse echo measurements," *Journal of the Acoustical Society of America*, 1991.
- [24] J. Goodman, *Statistical Optics*. John Wiley & Sons, 2015.